

# Arbitrary Analog/RF Spatial Filtering for Digital MIMO Receiver Arrays

Linxiao Zhang, *Student Member, IEEE*, and Harish Krishnaswamy<sup>1</sup>, *Member, IEEE*

**Abstract**—Traditional digital multiple-input multiple-output (MIMO) receivers that feature element-level digitization face high instantaneous dynamic range challenges in the analog/RF domain due to the absence of analog/RF spatial filtering. Existing analog/RF spatial notch filtering techniques are limited in their noise, linearity, and spatial filtering bandwidth performance. More importantly, only single spatial notches have been demonstrated, providing insufficient filtering in practical scenarios. We propose a frequency-translational arbitrary spatial filtering technique that features not only arbitrary spatial filtering response generation at baseband for the protection of the following analog-to-digital converters, but modulated baseband input impedance that can be translated by passive mixers to achieve arbitrary spatial filtering at RF as well. This technique allows the synthesis and independent steering of an arbitrary number of spatial notches, and the independent adjustment of notch depths. Current-mode operation leads to superior linearity performance and ultra-wideband rejection. A four-element 65-nm CMOS 0.1–3.1 GHz prototype MIMO receiver array shows arbitrary spatial response formation, more than 50-dB spatial rejection across all measured directions, and an ultra-wide 320-MHz 20-dB rejection bandwidth for a single-notch setting at 500-MHz local oscillator (LO) frequency. Formation of a single spatial notch only moderately degrades the equivalent single-element double-sideband noise figure from 2.1–3.7 dB to 3.4–5.8 dB. In the notch direction, +34 dBV in-band output-referred IP3 is measured, an improvement of 33 dB compared with outside-notch directions. A wireless demonstration shows the receiver array demodulating a weak spatial signal in the presence of two strong in-band spatial signals, verifying the arbitrary spatial filtering functionality.

**Index Terms**—Array signal processing, MIMO, notch filters, radio frequency, receivers, scalability, spatial diversity, spatial filters, spatial resolution.

## I. INTRODUCTION

MULTIPLE-INPUT multiple-output (MIMO) technology utilizes multiple antennas to achieve either spatial multiplexing gains [1], resulting in improved spectral efficiency, or diversity gain, resulting in improved link reliability [2], [3]. The improvement in spectral efficiency benefits from a larger scale in the MIMO system that is larger number of antennas, and therefore, massive MIMO has drawn a lot of attention for the next generation of wireless cellular networks (5G), particularly in a multi-user spatial multiplexing setting where a large number of antennas are used at the base

station to simultaneously communicate with a multitude of users [4].

Research on silicon-based multi-antenna systems has traditionally focused on linear beamforming or phased arrays, both at millimeter-wave frequencies [5]–[12] and in the sub-6-GHz RF range [13]–[17]. Such systems improve signal to noise ratio, resulting in only logarithmic increase in capacity with the number of antennas. As a preliminary work on MIMO systems, a spatio-temporal RAKE radar for vehicular applications exploits a passive multi-beamforming Butler matrix and orthogonal waveforms to simultaneously detect reflections from different directions as well as detect multipath reflections [18]. However, a Butler matrix does not allow flexible beam steering or frequency tuning. It is also bulky, making it hard to implement at lower RF frequencies.

MIMO communication systems typically require space-time array signal processing to leverage multiplexing and/or diversity gains. Such sophisticated signal processing can only be practically implemented in the digital domain [19]–[21]. Digital array processing also offers new opportunities for digital array calibration [22], [23]. However, since the array signal processing is accomplished in the digital domain, the RF/analog circuits together with the analog-to-digital converters (ADCs) have to handle the complete array aperture information. In the presence of strong and weak spatial signals, high instantaneous dynamic range is required, leading to high power consumption and cost.

In order to relax the ADC dynamic range requirement, RF/analog spatial filtering can potentially be recovered by utilizing analog multi-beamforming [24], [25]. For an MIMO system of  $N$  antennas, complex weightings  $A_{nn}$ , where  $n = 1, 2, \dots, N$ , can be applied to all antenna inputs to form  $N$  orthogonal beams, fully preserving the array aperture information, which can be used for digital array processing [Fig. 1(a)]. Alternatively, complex weightings  $B_{nn}$ , where  $n = 1, 2, \dots, N$ , can also be applied for the synthesis of spatial notches on all the outputs to suppress strong spatial signals [Fig. 1(b)]. However, all the RF and analog circuits before the output nodes are still exposed to strong spatial signals. Reference [26] uses couplers and an RF beamformer to extract a strong spatial signal and achieve (single) spatial notch filtering at RF, protecting the RF/analog circuits in addition to the following ADCs. However, integrated couplers degrade receiver noise performance, and are hard to implement at lower RF frequencies. The work in [27]–[29] synthesizes a baseband spatial notch impedance and frequency-translational RF front-ends translate the spatial notch filtering to RF. However, the spatial notch filter exploits voltage gain, showing both limited linearity and rejection

Manuscript received May 14, 2017; revised August 6, 2017 and September 24, 2017; accepted September 25, 2017. Date of publication November 1, 2017; date of current version November 21, 2017. This paper was approved by Guest Editor Alyosha Molnar. This work was supported by the DARPA ACT Program. (Corresponding author: Harish Krishnaswamy.)

The authors are with Department of Electrical Engineering, Columbia University, New York, NY 10027 USA (e-mail: harish@ee.columbia.edu).

Color versions of one or more of the figures in this paper are available online at <http://ieeexplore.ieee.org>.

Digital Object Identifier 10.1109/JSSC.2017.2759118

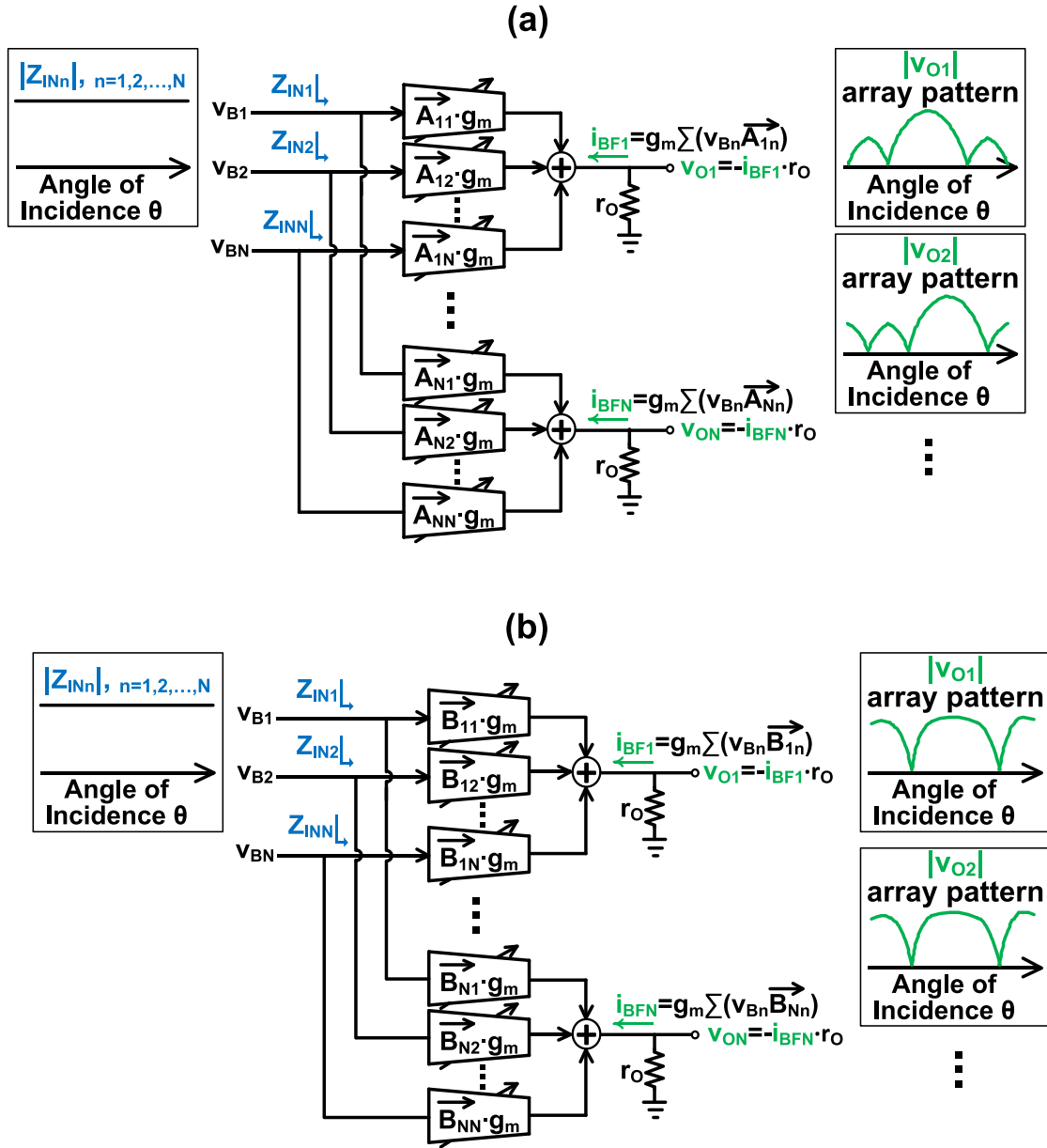


Fig. 1. Analog spatial filtering alternatives. (a) Multi-beamforming filtering. (b) Spatial notch filtering.

bandwidth in the notch direction. Fundamentally, both [26] and [27]–[29] only demonstrate single-notch suppression, which is insufficient in a practical wireless scenario where reflections and scattering in the channel can lead to complex and hostile power distribution in the spatial domain.

This paper introduces a frequency-translational arbitrary spatial filtering technique (FT-ASF) for digital MIMO receiver arrays that features not only arbitrary array pattern generation at the baseband outputs for the protection of the following ADCs, but modulated baseband input impedance that can be translated by passive mixers to achieve arbitrary spatial filtering at RF as well [30]. This technique allows the synthesis and independent steering of an arbitrary number of spatial notches, and the independent adjustment of notch depths. Current-mode operation leads to superior linearity performance and ultra-wideband rejection. The rest of this paper is organized as follows. Section II introduces the

proposed frequency-translational arbitrary spatial filtering technique, along with key building blocks. Section III describes the integrated circuit (IC) implementation of a prototype 0.1–3.1-GHz 65-nm CMOS four-element MIMO receiver array based on the proposed concepts. Section IV covers experimental results from the implemented prototype, and Section V concludes this paper.

## II. FREQUENCY-TRANSLATIONAL ARBITRARY SPATIAL FILTERING

In a multi-antenna receiver, signals may arrive from different directions at different power levels. While strong signals at different frequencies can be filtered out to a large extent in the RF/analog domain, the power levels of strong in-band signals can only be reduced by array signal processing based on their spatial information. If the power levels of spatially distinct signals can be made equal, or *spatially equalized*,



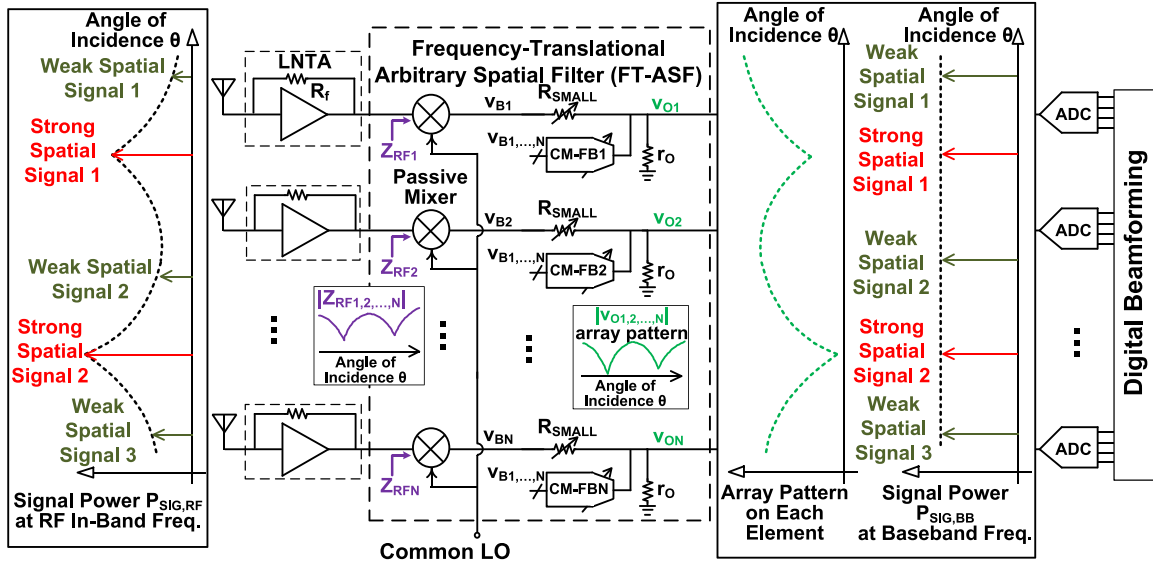


Fig. 3. Proposed MIMO receiver array featuring the frequency-translational arbitrary spatial filter (FT-ASF).

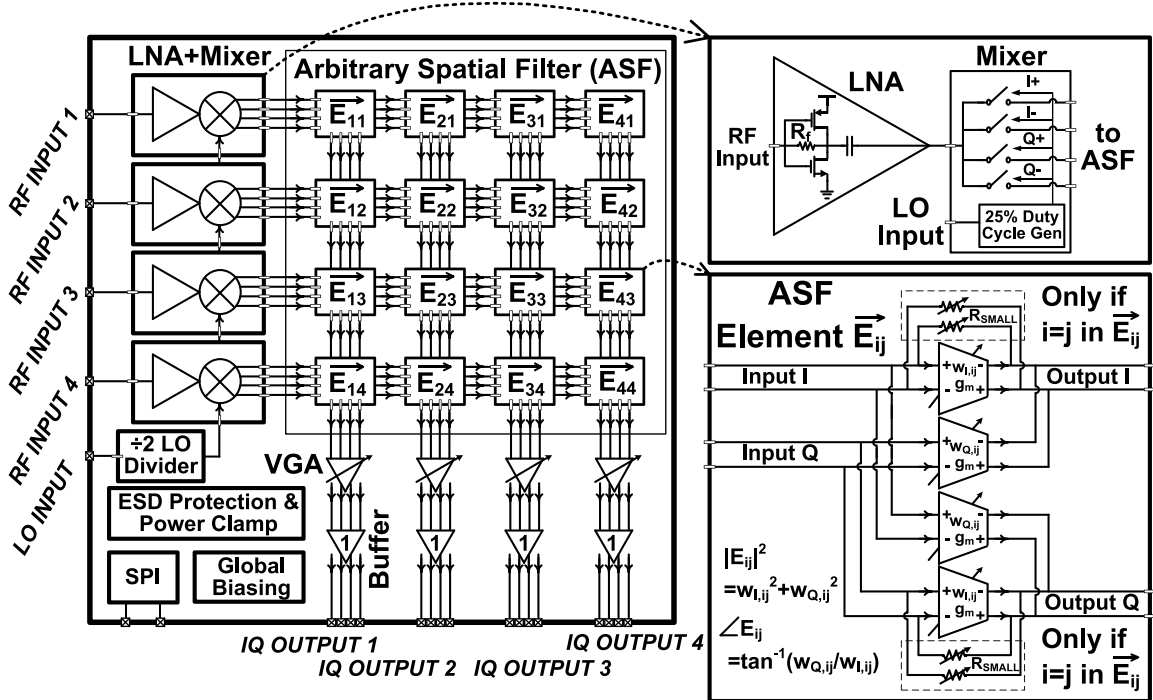


Fig. 4. Block diagram of the implemented four-element 65-nm CMOS 0.1–3.1 GHz MIMO receiver array featuring frequency-translational arbitrary spatial filtering.

respectively, in  $v_{O1,2,\dots,N}$ . Flexible CM-BFs with both phase and gain control allow the independent steering of one or more beams/nulls to arbitrary directions. If a certain value of rejection ratio is desired,  $i_{BF1,2,\dots,N}$  can also be synthesized to be a certain proportion of  $i_{B1,2,\dots,N}$ , therefore, allowing the flexible adjustment of notch depths in  $v_{O1,2,\dots,N}$  as well.

Since  $v_{O1,2,\dots,N}$  are given by (3), the baseband voltages  $v_{B1,2,\dots,N}$  can be easily found as

$$\begin{aligned} v_{B1,2,\dots,N} &= v_{O1,2,\dots,N} + i_{B1,2,\dots,N} \cdot R_{SMALL} \\ &= (i_{B1,2,\dots,N} - i_{BF1,2,\dots,N}) \cdot r_O + i_{B1,2,\dots,N} \cdot R_{SMALL}. \end{aligned} \quad (4)$$

And the input impedance,  $Z_{B1,2,\dots,N}$ , can be defined to be

$$Z_{B1,2,\dots,N} = \frac{v_{B1,2,\dots,N}}{i_{B1,2,\dots,N}} = R_{SMALL} + r_O \cdot \left(1 - \frac{i_{BF1,2,\dots,N}}{i_{B1,2,\dots,N}}\right). \quad (5)$$

Equation (5) shows that, in the directions of synthesized nulls in  $v_{O1,2,\dots,N}$ ,  $i_{BF1,2,\dots,N} = i_{B1,2,\dots,N}$  leads to virtual grounds at the output nodes, causing low input impedance  $Z_{B1,2,\dots,N} = R_{SMALL}$ . In the directions of synthesized beams in  $v_{O1,2,\dots,N}$ ,  $i_{BF1,2,\dots,N} = 0$  leads to high input impedance  $Z_{B1,2,\dots,N} = R_{SMALL} + r_O$ . In fact, the spatial response of the input impedances will follow that of the output voltages, except for a non-zero offset of  $R_{SMALL}$ . Intuitively, this offset



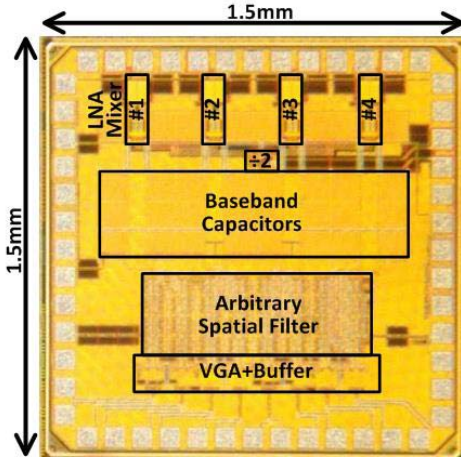


Fig. 5. Die micrograph.

is necessary so that  $v_{B1,2,\dots,N}$  are non-zero in null directions and can be sensed by the CM-BFs.

Given that the baseband input impedances  $Z_{B1,2,\dots,N}$  are modulated according to a desired spatial response, transparent passive mixers can translate these baseband impedances to RF frequencies, protecting the output nodes of the LNTAs and achieving arbitrary spatial filtering at RF. This unique feature of input impedance modulation differentiates the proposed FT-ASF from conventional architectures shown in the Fig. 1. In addition to the following ADCs, the proposed FT-ASF protects the baseband beamformers, passive mixers and the LNTA output nodes from strong spatial signal voltage swings as well, promising superior linearity.

Baseband input impedance modulation based on a desired spatial response is also achieved in [27]–[29], but only a single spatial notch can be synthesized at a time. Furthermore, low input impedances in the direction of a strong spatial signal are synthesized using baseband gyrators which exploit voltage gain. In other words, a strong spatial signal actually has to experience a large voltage gain to synthesize low input impedances, leading to degraded linearity. With the proposed FT-ASF, low input impedances are synthesized through current-mode operation, ensuring that strong spatial signals do not experience any voltage gain at any stage, promising superior linearity performance, which is verified by experimental results described in Section IV.

In order to accomplish a high spatial rejection ratio, a feed-forward structure is used in [27]–[29]. Since the signal path and the cancellation path are structurally very different, the cancellation bandwidth that can be achieved is limited. In fact, the cancellation bandwidth is limited by a high-impedance node on the cancellation path. On the other hand, in the proposed FT-ASF, the CM-BF output current  $i_{BFn}$  on the  $n$ th path can be written as

$$i_{BFn} = g_m \cdot \sum_{k=1}^N (\vec{E}_{nk} \cdot v_{Bk}) \quad (6)$$

where  $\vec{E}_{nk}$  are the complex weights associated with the beamforming in  $i_{BFn}$ . According to (5), the baseband current

$i_{Bn}$  on the  $n$ th path in notch directions is given by

$$i_{Bn} = v_{Bn,\text{notch}} / R_{\text{SMALL}}. \quad (7)$$

Equations (6) and (7) together with (3) lead to

$$v_{\text{On},\text{notch}} = v_{Bn,\text{notch}} \cdot r_O \cdot \left( \frac{1}{R_{\text{SMALL}}} - g_m \cdot \sum_{k=1}^N \left( \vec{E}_{nk} \cdot \frac{v_{Bk,\text{notch}}}{v_{Bn,\text{notch}}} \right) \right). \quad (8)$$

Matching across different elements indicates that  $(v_{Bk,\text{notch}}/v_{Bn,\text{notch}})$  is frequency-independent. If both  $g_m$  and  $\vec{E}_{nk}$  can be implemented in a frequency-independent fashion,  $v_{\text{On},\text{notch}}$  can be made equal to zero over wide bandwidths. Section III will show that  $\vec{E}_{nk}$  and  $g_m$  can be implemented to be frequency-independent, and Section IV will conform that ultra-wideband spatial filtering is indeed achieved.

An MIMO receiver array (Fig. 3) can be built based on this FT-ASF with superior linearity and ultra-wideband spatial filtering. Wideband LNTAs can be used to convert signals detected by antennas to RF currents, which in turn are down-converted by the following passive mixers before reaching the baseband arbitrary spatial filter. As mentioned earlier, the passive mixers will translate the modulated baseband input impedances to the LNTA outputs, offering arbitrary spatial filtering at RF as well. Such an MIMO receiver array can equalize the spatial signal power levels, while providing multiple baseband outputs to support digital beamforming. Flexible spatial filtering is performed early in the signal chain to protect the RF/analog circuits together with following ADCs. While LNTAs have been used in this paper to improve the noise performance, in principle, they can be removed to realize a mixer-first receiver array where the arbitrary spatial filtering is achieved at the antenna interface.

### III. CIRCUIT IMPLEMENTATION

An MIMO receiver array supporting RF/analog arbitrary spatial filtering is implemented in a 65-nm CMOS process (Figs. 4 and 5). This receiver array consists of four elements, each including an LNTA and a passive mixer. At baseband, a 4-input-4-output ASF is implemented. Automatic gain control functionality is ideally implemented separately from the ASF so that ASF resolution can be fully used for spatial filtering and to ease calibration. Following the ASF, we have implemented a variable-gain amplifier and a 50-Ω buffer for each output. While four elements are integrated on chip in this prototype, implementations with more elements may be considered, enabling sharper spatial filtering profiles.

#### A. RF Circuits

As explained in Section II, an FT-ASF is excited by RF currents provided by LNTAs. Inverter-based LNTAs are implemented for their high input-side linearity (Fig. 4). Since the FT-ASF provides high input impedances ( $R_{\text{SMALL}} + r_O$ ) in the directions of weak spatial signals which are translated to RF to load the LNTAs, resistive feedback is used to provide low-noise input matching. In the directions of strong spatial signals,

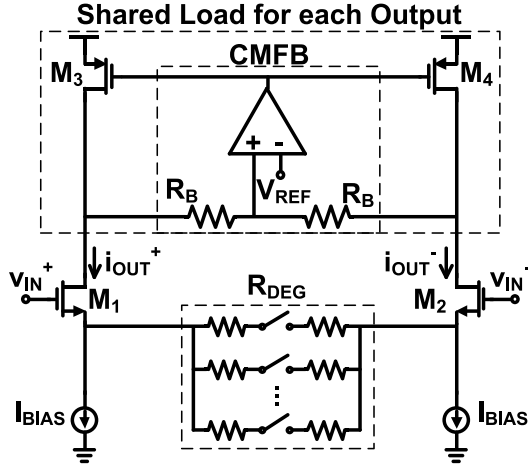
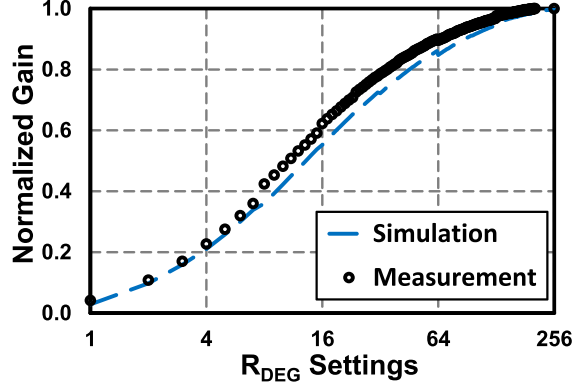


Fig. 6. Implemented tunable transconductance cell in the ASF with shared active load and CMFB, and its simulated and measured normalized gain as a function of  $R_{DEG}$  setting.



the LNTAs are loaded with a lower impedance translated by the passive mixer, causing the LNTAs to be partially reflective to the antennas.

A differential clock signal at twice the local oscillator (LO) frequency is generated off-chip. A clock frequency divider ( $\div 2$ ) is implemented on-chip to provide a 4-phase LO signal at the desired frequency, which is distributed to 4 identical single-balanced I/Q passive mixers, driven by the 4 LNTAs. Within each mixer, a digital duty cycle generator reduces the LO signal duty cycle from 50% to slightly less than 25% to ensure the non-overlapping switching of the mixer switches (Fig. 4). At the mixer output nodes, large shunt metal-insulator-metal capacitors filter out out-of-band signals.

### B. Arbitrary Spatial Filter

The implemented 4-input-4-output ASF consists of 16 elements,  $\vec{E}_{11}$  through  $\vec{E}_{44}$ , where the  $\vec{E}_{ij}$  element senses the baseband voltage on the  $j$ th element and converts it to a current to the  $i$ th output with a complex gain of  $\vec{E}_{ij}$ . In the four elements where  $i = j$ , small resistors  $R_{SMALL}$  are inserted in parallel to achieve the input impedance modulation explained in Section II.

Within the  $\vec{E}_{ij}$  element, the complex gain  $\vec{E}_{ij}$  is achieved by weighting the I-path  $g_m$  cell and Q-path  $g_m$  cell differently,  $w_{I,ij}$  and  $w_{Q,ij}$ , and combining the  $g_m$  cell output currents together. This structure is conceptually similar to the Cartesian phase shifter used in [27]–[29]. The phase shift achieved is given by  $\angle \vec{E}_{ij} = \tan^{-1}(w_{Q,ij}/w_{I,ij})$ , and at the same time, magnitude control of  $\vec{E}_{ij}$  is also embedded, as given by  $E_{ij} = |\vec{E}_{ij}| = (w_{Q,ij}^2 + w_{I,ij}^2)^{1/2}$ . Two tunable  $g_m$  cells are also used for the Q-path output of the  $\vec{E}_{ij}$  element.

The circuit diagram of the tunable  $g_m$  cells, together with the shared active load and common-mode feedback (CMFB) circuit for each output, is shown in Fig. 6. Since the ASF appears in the baseband after front-end LNTA gain, we have prioritized linearity over noise in its design. Each  $g_m$  cell consists of an nMOS differential pair with tunable resistive degeneration resistor  $R_{DEG}$ . Bias currents do not flowthrough

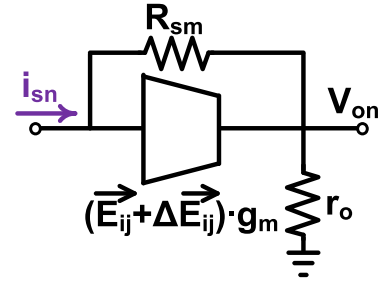
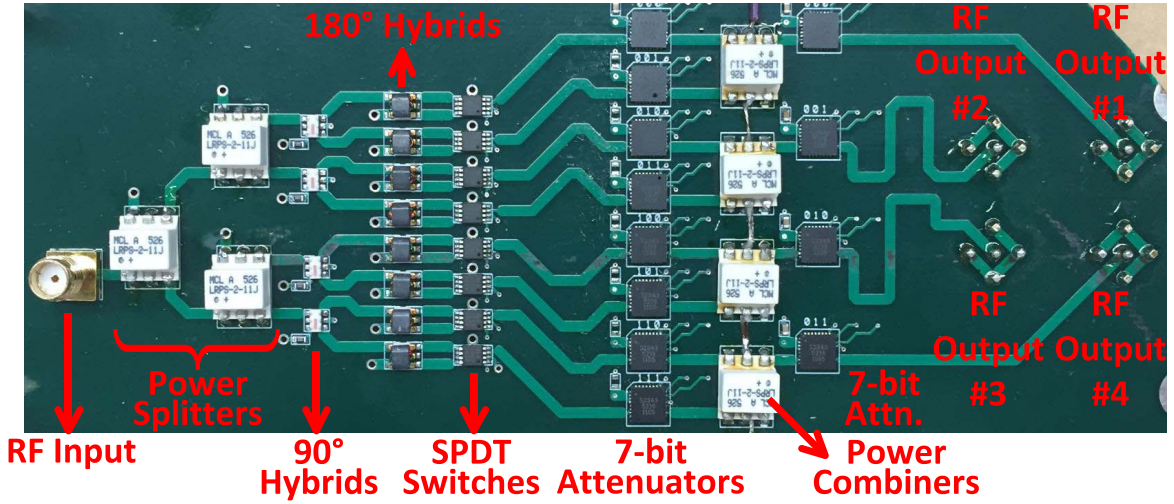


Fig. 7. Equivalent circuit of ASF showing complex weighting error  $\Delta \vec{E}_{ij}$ .

the degeneration resistor  $R_{DEG}$ , saving voltage headroom for higher linearity. However, the two current sources contribute noise to differential mode signal unlike a common-mode current source. Also, even though  $R_{DEG}$  can be made large, the finite output resistance of the current sources limits the  $g_m$  tuning range at dc. The smallest transconductance gain that can be achieved is 23.5-dB smaller than the maximum gain. The tuning step from zero gain, namely, when the  $g_m$  cell is turned off, to the minimum gain setting when the  $g_m$  cell is turned on, is the largest tuning step and therefore determines the effective number of bits of the magnitude control. 3.9 bit of magnitude control is achieved with this  $g_m$  cell.

From the magnitude control resolution, one can determine the phase control resolution imposed by the different magnitude control settings on the I-path and Q-path  $g_m$  cells. Assuming all  $g_m$  cells are perfectly matched, the largest phase shift step is from  $0^\circ$ , when the I-path  $g_m$  is at its maximum setting and the Q-path  $g_m$  is off, to the phase shift when the Q-path  $g_m$  is increased to its minimum non-zero transconductance gain. This largest phase shift step is  $3.8^\circ$  with the given implementation, equivalent to 6.5 effective bits of phase control.

Knowing the resolution of both the magnitude control and the phase controls, one can calculate the theoretical minimum rejection ratio (notch depth) that can be achieved. Outside the notch direction, the baseband CM-BFs draw negligible amount of current. So the  $n$ th ASF output voltage in Fig. 7 is



### Calibration Results:

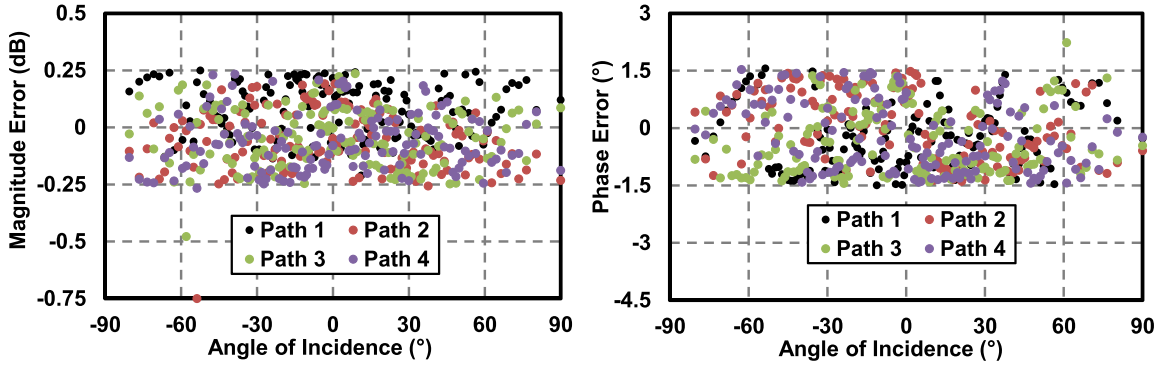


Fig. 8. 4-path wideband RF phase shifter PCB that is used in the measurements to mimic a uniform linear antenna array. Its calibration results show magnitude errors mostly within  $\pm 0.25$  dB and phase errors mostly within  $\pm 1.5^\circ$  at 502 MHz.

given by

$$v_{\text{on},\text{OON}} = i_{\text{sn}} \cdot r_o \quad (9)$$

where  $i_{\text{sn}}$  is the output current of the  $n$ th RF front-end and  $r_o$  is the output resistance of the baseband beamformer.

Assuming all  $g_m$  cells are perfectly matched and a single broadside notch is to be formed, in Fig. 7, we must have  $\vec{E}_{ij} g_m R_{\text{sm}} = 1 \angle 0^\circ$ . Circuit analysis reveals that the  $n$ th ASF output voltage in the notch direction is given by

$$v_{\text{on},\text{IN}} = -i_{\text{sn}} R_{\text{sm}} \frac{\Delta \vec{E}_{ij}}{\vec{E}_{ij}} \left/ \left( 1 + \frac{\Delta \vec{E}_{ij}}{\vec{E}_{ij}} \right) \right. \approx -i_{\text{sn}} R_{\text{sm}} \frac{\Delta \vec{E}_{ij}}{\vec{E}_{ij}} \quad (10)$$

where  $\Delta \vec{E}_{ij}$  is the error vector due to the worst case magnitude and phase errors, and  $\vec{E}_{ij} g_m$  is the sum of the transconductance gain of all the  $g_m$  cells connected to the output node of interest. Note that  $E_{ij} g_m r_o$  is equal to the intrinsic gain of the  $g_m$  cells used, where  $E_{ij}$  is the magnitude of  $\vec{E}_{ij}$ . So, the rejection ratio  $RR_{\text{min}}$  can be predicted as

$$RR_{\text{min}} = \left| \frac{v_{\text{on},\text{IN}}}{v_{\text{on},\text{OON}}} \right| = \frac{i_{\text{sn}} R_{\text{sm}} \frac{\Delta E_{ij}}{E_{ij}}}{i_{\text{sn}} \cdot r_o} = \frac{\Delta E_{ij}}{E_{ij}} \cdot \frac{1}{E_{ij} g_m r_o}. \quad (11)$$

This equation shows that, in addition to the resolution of the ASF ( $\Delta E_{ij}/E_{ij}$ ), the modulation of the input resistance

( $R_{\text{sm}}/r_o$ ) =  $(1/E_{ij} g_m r_o)$ , which is the inverse of the intrinsic gain, also contributes to the overall rejection ratio. In this design, as mentioned earlier, 3.9 bit of magnitude control and 6.5 bit of phase control are available, and the baseband  $g_m$  cells have an intrinsic gain of about 26 dB (non-minimum channel lengths are used). Equation (11) predicts a worst case rejection ratio of  $-50.3$  dB. Section IV shows that the measured rejection ratios for single-notch settings are consistent with this prediction.

## IV. EXPERIMENTAL RESULTS

The implemented IC is packaged in a commercial 64-pin QFN package. Unless otherwise stated, the receiver array is assumed to be excited by a linear uniform antenna array with  $\lambda_{LO}/2$  spacing (where  $\lambda_{LO}$  corresponds to the wavelength in free space at the LO frequency).

To mimic a uniform linear antenna array excitation with precise magnitude and phase control, a four-path wideband RF phase shifter PCB is designed (Fig. 8). On this PCB, power splitters divide the input RF signal four ways, and is followed in each path by a  $90^\circ$  hybrid to provide I/Q signals,  $180^\circ$  hybrids to provide both polarities, and single-pole-double-throw (SPDT) switches for the polarity selection. Two 7-bit attenuators then weight the I/Q branches on each



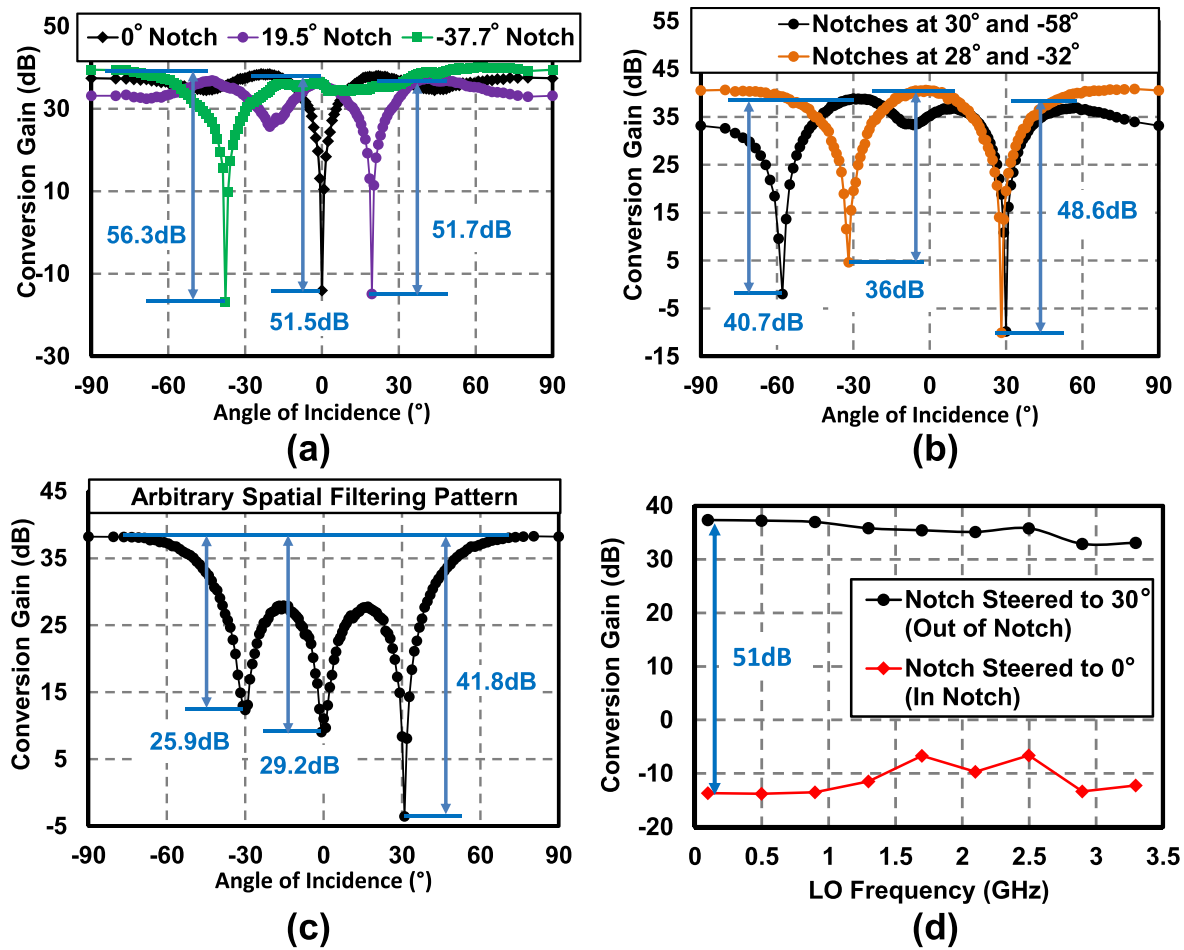


Fig. 9. In-band conversion gain of element 4 of the receiver array at 500-MHz LO is shown across angle of incidence for different FT-ASF settings. (a) Single notch steered to different directions. (b) Two simultaneous notches steered to different directions. (c) Three notches with variable notch depth. (d) With a single notch steered to broadside ( $0^\circ$ ) and  $+30^\circ$ , in-band conversion gain in the broadside direction across LO frequencies is also shown.

path independently followed by a power combiner that creates the phased-shifted signal based on the I/Q weightings. An attenuator is then used on each path to create one more degree of freedom to equalize the magnitudes of the four phased-shifted signals before they are used to drive the implemented MIMO receiver array. All of the SPDT switches and the attenuators are controlled digitally with a micro-controller from a computer. VNA-based calibration is carried out to ensure that the magnitudes are equal on all outputs, and desired progressive phase offset can be synthesized across the four outputs. Careful iterative calibration leads to magnitude errors mostly within  $\pm 0.25$  dB, and phase errors mostly within  $\pm 1.5^\circ$  at 502 MHz. The operation bandwidth of the phase-shifter is 300–700 MHz, limited by the  $90^\circ$  hybrid. At frequencies other than 502 MHz, calibration is carried out only for a few angles of incidence, such as the broadside angle ( $0^\circ$ ) and  $+30^\circ$ . Unless otherwise indicated, all of the measurements are carried out with this phase shifter PCB.

At 500 MHz LO, in-band conversion gain at 502 MHz RF frequency (2 MHz baseband frequency) across angles of incidence is measured (results for the fourth element are shown). The implemented MIMO receiver array is configured to form a single spatial notch, which can be freely

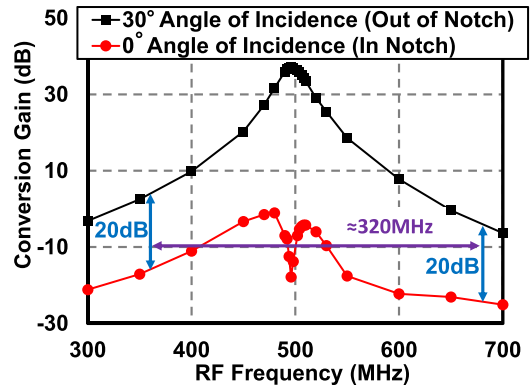


Fig. 10. Measured ultra-wideband spatial filtering with 500-MHz LO and a single spatial notch steered to broadside ( $0^\circ$ ).

steered to an arbitrary direction. Fig. 9(a) shows three array patterns, each achieving a single spatial notch pointing to a different direction with  $>51$ -dB notch depth, consistent with the achievable notch depth predicted in Section III. If multiple strong spatial signals are present, multiple independent spatial notches can be formed as well. For example, two spatial notches are formed in Fig. 9(b). In this example, a spatial notch can be steered from  $-58^\circ$  to  $-32^\circ$  while a second spatial



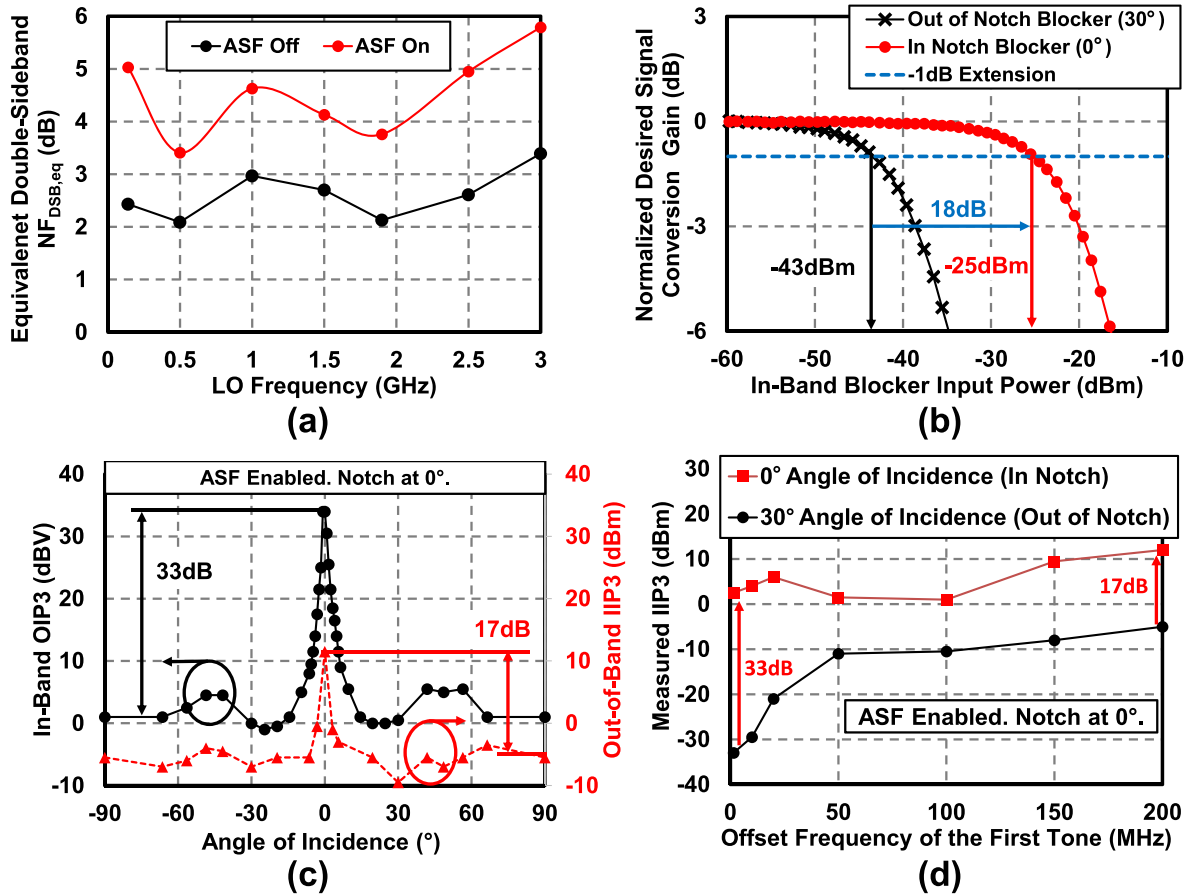


Fig. 11. (a) Measured equivalent double-sideband noise figure,  $NF_{DSB,eq}$ , is reported across LO frequency with the spatial equalizer on (single spatial notch steered to  $+30^\circ$ ) and off. (b) In-band blocker power level at which a small out-of-notch desired signal is compressed by 1 dB is shown for in-notch and out-of-notch incidence. (c) and (d) IIP3 and OIP3 are also shown for two tones with varying angle of incidence and frequency offset.

notch is kept at approximately  $+30^\circ$ . With the four-element FT-ASF, a maximum of 3 notches can be formed, as shown in Fig. 9(c), and here, the ability to engineer independent notch depths is also showcased. In general, the synthesis of a completely arbitrary array pattern is only limited by the scale of the receiver array. The mathematical method for generating the complex weightings for the 16 ASF elements is similar to that of an adaptive beamformer, which has been studied extensively in the literature [31]. In order to generate these measurements, the I and Q gain profiles of a single channel are measured as a function of digital code. The profiles are then assumed to be identical across all elements to generate the initial complex weightings. Element-to-element variations limit the resultant array patterns, and a search around this nominal setting is performed to obtain the desired notches. The design of  $g_m$  cells that have more linear gain control and are more resilient to mismatch, as well as efficient calibration algorithms, represent topics for future research.

In order to show the spatial notch depth across LO frequency, a broadband four-way passive power splitter is used to mimic a linear uniform antenna array excited from the broadside ( $0^\circ$ ) direction. First, a single spatial notch is steered to  $+30^\circ$ , leaving the broadside excitation outside the notch. High in-band conversion gain at 2 MHz baseband frequency

is consistently measured across the 0.1–3.1-GHz LO frequency range. Next, if the spatial notch is steered to broadside, rejecting the excitation, the receiver array shows attenuation.  $>40$ -dB rejection ratio is measured throughout the entire 0.1–3.1-GHz LO frequency range [Fig. 9(d)].

At 500-MHz LO with a single spatial notch steered to the broadside ( $0^\circ$ ) direction, receiver array conversion gain is measured across RF frequency from 300 to 700 MHz (again showing results for the fourth element) (Fig. 10). If a signal arrives at  $+30^\circ$ , which is outside the spatial notch, it experiences high conversion gain at in-band frequencies, and high-Q bandpass filtering. However, if this signal arrives at the broadside ( $0^\circ$ ) direction, which is inside the spatial notch, it only experiences attenuation, regardless of its RF frequency. Comparing these frequency responses, high spatial suppression is consistently measured across frequency, even at out-of-band frequencies where spectral filtering already exists.  $>20$ -dB spatial filtering is measured over  $\approx 320$  MHz. At far out-of-band frequencies, the spatial filtering degrades, possibly because of the fact that in the tunable  $g_m$  cells used in the ASF, both the parasitic capacitive loading on the differential pair source nodes and the gate-to-drain parasitic capacitive coupling of the differential pair devices are frequency-dependent, degrading the current cancellation accuracy at the  $g_m$  cell

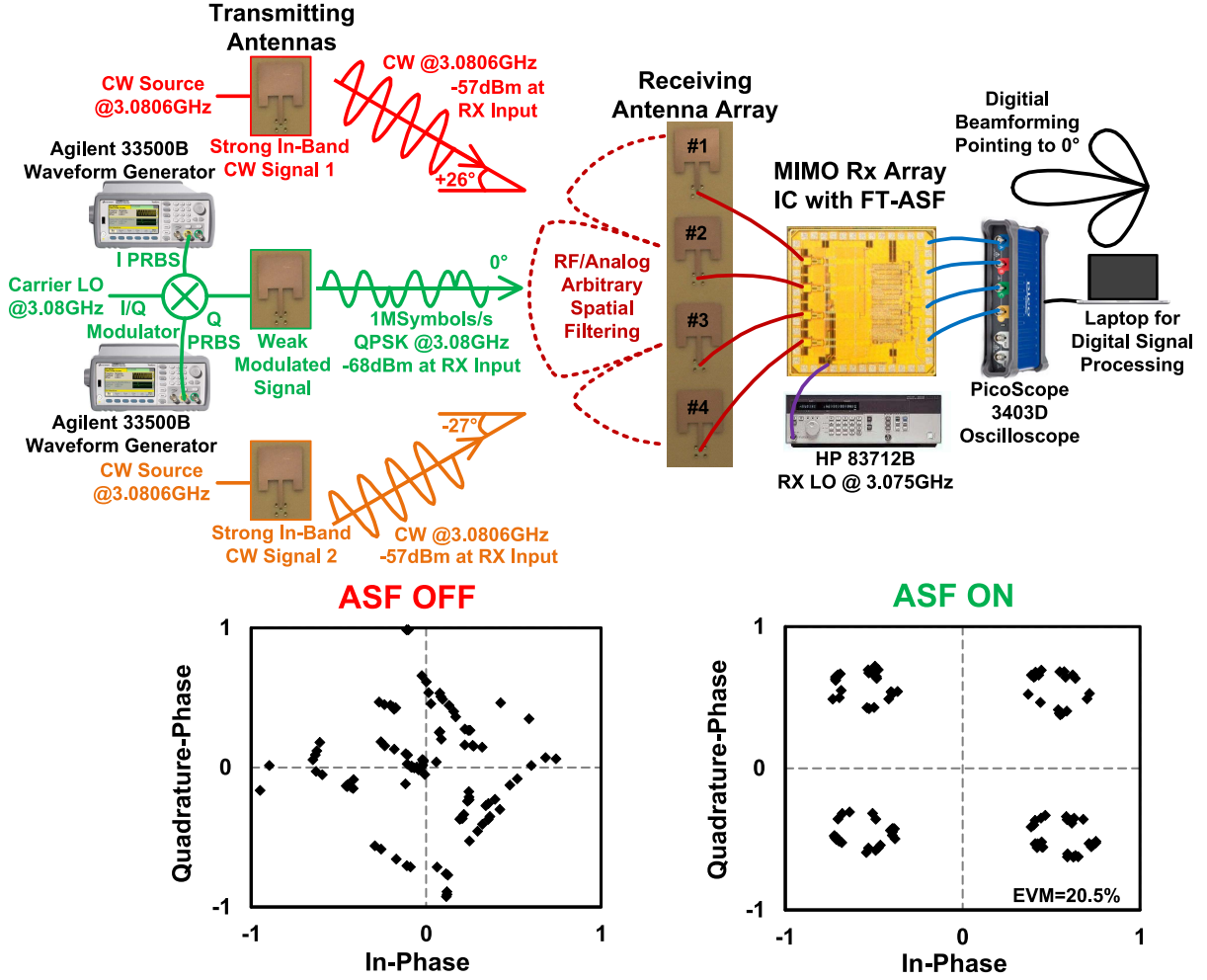


Fig. 12. 3-GHz wireless demo is depicted, where arbitrary spatial filtering enables the suppression of two in-band powerful CW signals to successfully receive a desired 11-dB-weaker QPSK signal.

output nodes at high baseband frequencies. It should also be noted that the broadside ( $0^\circ$ ) excitation eliminates the delay-phase approximation error faced by all phased-array systems. If the excitation arrives from directions other than broadside, the spatial filtering bandwidth is expected to degrade.

The noise performance of the implemented MIMO receiver array can be characterized with the equivalent single-element double-sideband noise figure ( $NF_{DSB,eq}$ ) concept introduced in [27]–[29]. At the LO frequency of interest, one of the four elements is excited with a noise source while the other three elements are terminated with noisy  $50\ \Omega$  terminations. The four baseband output signals from the MIMO array are used to point a beam to a direction outside the spatial notch, representing a weak spatial signal that requires good receiver sensitivity. The measured beamformed double-sideband noise figure  $NF_{DSB,BF}$  can be referred back to the four-element receiver array outputs by adding 6 dB. Furthermore, since only one element is excited instead of four, leading to a 12-dB SNR degradation, this SNR degradation has to be subtracted from  $NF_{DSB,BF}$  to represent the noise figure of an equivalent single receiver element when excited by a linear uniform antenna array. In this case, a spatial notch is steered

to  $+30^\circ$  and a four-way power combiner at baseband is used to form a beam pointing to the broadside ( $0^\circ$ ) direction. Measured  $NF_{DSB,eq}$  is shown across LO frequency in Fig. 11(a). First, the ASF is disabled by turning off all the  $g_m$  cells in it, and measured  $NF_{DSB,eq}$  ranges from 2.1 to 3.7 dB in the 0.1–3.1-GHz LO frequency range. Note that in this mode of operation, the elements in the implemented receiver array do not have any interaction. Hence, each receiver element can be individually measured, and the same NF is measured as  $NF_{DSB,eq}$ , working as a sanity check. Once a single  $+30^\circ$  notch is formed for all the four outputs, measured  $NF_{DSB,eq}$  shows a moderate degradation, ranging from 3.4 to 5.8 dB. In both cases,  $NF_{DSB,eq}$  degrades at low LO frequencies due to the finite size of the dc-blocking capacitors used at the output of the LNTAs. At high LO frequencies, LNTA and mixer parasitic capacitances degrade LNTA gain.

At 500-MHz LO, blocker P1-dB measurement is carried out for an in-band in-notch spatial blocker. A four-way power splitter provides an in-band broadside excitation at variable power levels, while the phase-shifter PCB is used to provide an in-band  $+30^\circ$  excitation at a constant power level, representing a desired weak spatial signal. The normalized conversion gain

	ISSCC, 2013 [15]	ISSCC, 2014 [16]	RFIC, 2016 [26]	JSSC, 2016 [29]	This Work
<b>Functionality</b>	MISO Phased Array	MISO Phased Array	MIMO with Single Spatial Notch	MIMO with Single Spatial Notch	<b>MIMO with FT-ASF</b>
<b>CMOS Process</b>	65nm	65nm	65nm	65nm	<b>65nm</b>
<b>Chip Area (mm<sup>2</sup>)</b>	2.25/0.97 <sup>1</sup>	1.06/0.2 <sup>1</sup>	3.8	2.25/1.69 <sup>1</sup>	<b>2.25/1.44<sup>1</sup></b>
<b>Supply Voltage (V)</b>	1.2	1	1.3 - 1.5	1.2	<b>1.2</b>
<b>Number of Inputs/Outputs</b>	4/1	4/1	4/1 <sup>17</sup>	4/4	<b>4/4</b>
<b>RF Operating Frequency Range (GHz)</b>	0.6 - 3.6	1 - 2.5	10	0.1 - 1.7	<b>0.1 - 3.1</b>
<b>Single-element Conversion Gain (dB)</b>	-1 <sup>2</sup>	12	14	41	<b>43</b>
<b>Equivalent Single-element NF<sub>DSB,eq</sub><sup>3</sup> (dB)</b>	5-8 <sup>4</sup>	6	8 <sup>5</sup> 9.5 <sup>18</sup>	1.7 - 4.5 <sup>5</sup> 2.2-4.6 <sup>6</sup>	<b>2.1 - 3.4<sup>7</sup> 3.4 - 5.8<sup>8</sup></b>
<b>Spatial Suppression (dB)</b>	38	NR	32 <sup>16</sup>	32	<b>51 - 56<sup>10</sup></b>
<b>20dB Spatial Suppression BW (MHz/%)</b>	NR	NR	100/1%	15/3% <sup>15,16</sup>	<b>320/64%<sup>15</sup></b>
<b>In-Band OIP3<sup>11</sup> (dBV)</b>	-9 - -2 <sup>12</sup>	+3	NR	-10 <sup>12</sup> +24 <sup>13</sup>	<b>+1<sup>12</sup> +34<sup>13</sup></b>
<b>Out-of-Band IIP3<sup>11</sup> (dBm)</b>	+20 <sup>14,9</sup>	+5	NR	+11 <sup>12</sup> +18 <sup>13</sup>	<b>-5<sup>12</sup> +12<sup>13</sup></b>
<b>Power Consumption (4-element, mW)</b>	68 - 195	26 - 36	145 <sup>17</sup>	140-160 Over 0.1-1.7GHz	<b>116-147 Over 0.1-3.1GHz</b>
NR Not reported. <sup>1</sup> Active area. <sup>2</sup> Reported by [ISSCC,2014] <sup>3</sup> Equivalent Single-Element NF <sub>DSB,eq</sub> = NF <sub>DSB</sub> measured with single-element excitation and output side beamforming - 10log(# of elements). <sup>4</sup> [ISSCC, 2013] reports single-element NF <sub>DSB</sub> as 3-6dB but only 4dB SNR improvement is seen in the array. <sup>5</sup> Spatial notch off. <sup>6</sup> Spatial notch on. <sup>7</sup> ASF off. <sup>8</sup> ASF on. <sup>9</sup> Single-element measurement. <sup>10</sup> Single-notch settings. <sup>11</sup> Power is referred to single-element input/output. <sup>12</sup> Receiving angle. <sup>13</sup> Rejecting angle. <sup>14</sup> from JSSC follow-up paper. <sup>15</sup> For a single broadside notch at 500MHz LO. <sup>16</sup> Estimated based on figure. <sup>17</sup> Only one antenna has the entire RF signal path implemented, but 4 inputs are implemented for spatial cancellation. <sup>18</sup> There is 1.5dB noise increase when cancellation is on.					

Fig. 13. Performance summary and comparison to the state of the art.

of the weak desired signal is shown as a function of the broadside blocker power level in Fig. 11(b). With the ASF turned off, the measured blocker P1 dB is -43 dBm. Once a broadside spatial notch is synthesized by the ASF, the measured blocker P1 dB improves to -25 dBm, representing an 18-dB improvement.

At 500-MHz LO, two tone tests are carried out across angle of incidence and frequency [Fig. 11(c) and (d)] with a single spatial notch steered to the broadside (0°) direction. At in-band frequencies, output-referred IP3 (OIP3)<sup>1</sup> is reported across angle of incidence. The measured OIP3 is improved from +1-dBV outside the spatial notch to +34 dBV in the spatial notch direction. At out-of-band frequencies, input-referred IP3 (IIP3) is reported. At 200-MHz offset, the measured IIP3 is improved from -5 dBm outside the notch to +12 dBm in the spatial notch direction. The measured IIP3 is shown in Fig. 11(d) for both in-notch and outside-notch directions as a function of the test tone frequency offset. At in-band

frequencies, IIP3 is improved by +33 dB, while at out-of-band frequencies, the improvement is +17 dB.

In order to demonstrate the unique feature of arbitrary spatial filtering, a wireless demonstration is carried out (Fig. 12). A four-element linear uniform antenna array with  $\lambda/2$  spacing at 3.08 GHz is designed and fabricated. This antenna array is used to excite the implemented four-element MIMO receiver array. A four-channel oscilloscope is used to digitize the four array outputs for digital processing. A laptop computer is used to control both the receiver array IC and the 4-channel oscilloscope, as well as to perform the digital signal processing. On the transmitting side, a 1-MSample/s QPSK signal is generated at 3.08 GHz and irradiated toward the broadside direction of the antenna array. This modulated signal has a power level of -68 dBm at the receiver array input at each element. At the same time, two continuous-wave (CW) signals generated at 600-kHz offset from the modulated signal center frequency are irradiated from +26° and -27°, respectively, each of them having 11-dB higher power than the modulated signal. The receiver array IC is configured to provide maximum gain. Without the ASF functionality, both CW signals experience the high conversion gain and saturate the following oscilloscope, leaving the modulated signal

<sup>1</sup>At in-band frequencies, baseband output nodes typically limit linearity because of the high gain. Consequently, gain is important to specify in addition to in-band IIP3, or alternatively, OIP3 can be specified. At out-of-band frequencies, filtering will eliminate the signal down the chain and therefore, IIP3 can be used for comparison.

impossible to demodulate. With the ASF functionality, two spatial notches can be formed to point to the two CW signals, reducing their power levels so that the following oscilloscope is no longer saturated. Further digital beamforming provides sufficient spatial filtering to demodulate the weaker modulated signal, showing a clean constellation and an error vector magnitude (EVM) of 20.5%. The arbitrary spatial filtering provided by the implemented MIMO receiver array IC in this demonstrator is limited by the calibration algorithms employed. Improved iterative calibration algorithms can lead to lower demodulated signal EVM in the presence of stronger spatial blockers.

## V. CONCLUSION

Fig. 13 compares this paper with the state-of-the-art CMOS multiple-antenna receivers. References [15], [16] are phased-array receivers at sub-6-GHz operating frequency. References [26], [29] are MIMO receivers capable of forming a single analog/RF spatial notch. To the best of our knowledge, this paper is the only MIMO receiver array that demonstrates arbitrary spatial filtering in the RF/analog domain, supporting multiple independent spatial notches. The spatial suppression ratio achieved with a single notch setting is considerably higher than the state of the art, and the suppression bandwidth is superior as well, absolute valuwewise or percentagewise. Due to the current-mode operation and the spatially modulated ASF input impedance, the in-band OIP3 achieved is higher than the state of the art, while the out-of-band IIP3 is also competitive. The noise performance achieved is either comparable or superior to the state of the art as well.

This paper presented a frequency-translational arbitrary spatial filtering technique in the RF and analog domain for digital MIMO receiver arrays that provides high suppression ratio, ultra-wide suppression bandwidth and high in-/out-of-band linearity. Experimental results are reported from a 0.1–3.1-GHz four-element MIMO receiver array IC prototype implemented in a 65-nm CMOS technology. Further research on arbitrary spatial filtering techniques, including scalable spatial filtering and algorithms for efficient array calibration, is critical for the deployment of cost-effective, power-efficient, and large-scale MIMO technology.

## REFERENCES

- [1] G. J. Foschini, "Layered space-time architecture for wireless communication in a fading environment when using multi-element antennas," *Bell Labs Tech. J.*, vol. 1, no. 2, pp. 41–59, 1996.
- [2] S. M. Alamouti, "A simple transmit diversity technique for wireless communications," *IEEE J. Sel. Areas Commun.*, vol. 16, no. 8, pp. 1451–1458, Oct. 1998.
- [3] V. Tarokh, N. Seshadri, and A. R. Calderbank, "Space-time codes for high data rate wireless communication: Performance criterion and code construction," *IEEE Trans. Inf. Theory*, vol. 44, no. 2, pp. 744–765, Mar. 1998.
- [4] E. G. Larsson, O. Edfors, F. Tufvesson, and T. L. Marzetta, "Massive MIMO for next generation wireless systems," *IEEE Commun. Mag.*, vol. 52, no. 2, pp. 186–195, Feb. 2014.
- [5] A. Natarajan, A. Komijani, and A. Hajimiri, "A fully integrated 24-GHz phased-array transmitter in CMOS," *IEEE J. Solid-State Circuits*, vol. 40, no. 12, pp. 2502–2514, Dec. 2005.
- [6] X. Guan, H. Hashemi, and A. Hajimiri, "A fully integrated 24-GHz eight-element phased-array receiver in silicon," *IEEE J. Solid-State Circuits*, vol. 39, no. 12, pp. 2311–2320, Dec. 2004.
- [7] A. Babakhani, G. Xiang, A. Komijani, A. Natarajan, and A. Hajimiri, "A 77-GHz phased-array transceiver with on-chip antennas in silicon: Receiver and antennas," *IEEE J. Solid-State Circuits*, vol. 41, no. 12, pp. 2795–2806, Dec. 2006.
- [8] A. Valdes-Garcia *et al.*, "A fully integrated 16-element phased-array transmitter in SiGe BiCMOS for 60-GHz communications," *IEEE J. Solid-State Circuits*, vol. 45, no. 12, pp. 2757–2773, Dec. 2010.
- [9] K.-J. Koh and G. M. Rebeiz, "An X- and Ku-band 8-element phased-array receiver in 0.18- $\mu\text{m}$  SiGe BiCMOS technology," *IEEE J. Solid-State Circuits*, vol. 43, no. 6, pp. 1360–1371, Jun. 2008.
- [10] H. Krishnaswamy and H. Hashemi, "A 4-channel 24–27 GHz UWB phased array transmitter in 0.13  $\mu\text{m}$  CMOS for vehicular radar," in *Proc. IEEE Custom Integr. Circuits Conf.*, Sep. 2007, pp. 753–756.
- [11] H. Krishnaswamy and H. Hashemi, "A variable-phase ring oscillator and PLL architecture for integrated phased array transceivers," *IEEE J. Solid-State Circuits*, vol. 43, no. 11, pp. 2446–2463, Nov. 2008.
- [12] Y. Pei, Y. Chen, D. M. W. Leenaerts, and A. H. M. van Roermund, "A 30/35 GHz dual-band transmitter for phased arrays in communication/radar applications," *IEEE J. Solid-State Circuits*, vol. 50, no. 7, pp. 1629–1644, Jul. 2015.
- [13] R. Tseng, H. Li, D. H. Kwon, Y. Chiu, and A. S. Y. Poon, "A four-channel beamforming down-converter in 90-nm CMOS utilizing phase-oversampling," *IEEE J. Solid-State Circuits*, vol. 45, no. 11, pp. 2262–2272, Nov. 2010.
- [14] M. C. M. Soer, E. A. M. Klumperink, B. Nauta, and F. E. van Vliet, "A 1.0-to-4.0 GHz 65 nm CMOS four-element beamforming receiver using a switched-capacitor vector modulator with approximate sine weighting via charge redistribution," in *IEEE Int. Solid-State Circuits Conf. (ISSCC) Dig. Tech. Papers*, Feb. 2011, pp. 64–66.
- [15] A. Ghaffari, E. E. A. M. Klumperink, F. van Vliet, and B. Nauta, "Simultaneous spatial and frequency-domain filtering at the antenna inputs achieving up to +10 dBm out-of-band/beam  $P_{1dB}$ ," in *IEEE Int. Solid-State Circuits Conf. (ISSCC) Dig. Tech. Papers*, Feb. 2013, pp. 84–85.
- [16] M. C. M. Soer, E. A. M. Klumperink, B. Nauta, and F. E. van Vliet, "A 1.0-to-2.5 GHz beamforming receiver with constant-Gm vector modulator consuming <9 mW per antenna element in 65 nm CMOS," in *IEEE Int. Solid-State Circuits Conf. (ISSCC) Dig. Tech. Papers*, Feb. 2014, pp. 66–67.
- [17] M. C. M. Soer, E. A. M. Klumperink, D.-J. van den Broek, B. Nauta, and F. E. van Vliet, "Beamformer with constant-Gm vector modulators and its spatial intermodulation distortion," *IEEE J. Solid-State Circuits*, vol. 52, no. 3, pp. 735–746, Mar. 2017.
- [18] H. Krishnaswamy and H. Hashemi, "A 4-channel 4-beam 24-to-26 GHz spatio-temporal RAKE radar transceiver in 90 nm CMOS for vehicular radar applications," in *IEEE Int. Solid-State Circuits Conf. (ISSCC) Dig. Tech. Papers*, Feb. 2010, pp. 214–215.
- [19] N. Klemmer *et al.*, "A 45 nm CMOS RF-to-bits LTE/WCDMA FDD/TDD 2 $\times$ 2 MIMO base-station transceiver SoC with 200 MHz RF bandwidth," in *IEEE Int. Solid-State Circuits Conf. (ISSCC) Dig. Tech. Papers*, Jan. 2016, pp. 164–165.
- [20] Y. Palaskas *et al.*, "A 5-GHz 108-Mb/s 2  $\times$  2 MIMO transceiver RFIC with fully integrated 20.5-dBm  $P_{1dB}$  power amplifiers in 90-nm CMOS," *IEEE J. Solid-State Circuits*, vol. 41, no. 12, pp. 2746–2756, Dec. 2006.
- [21] M. He *et al.*, "A 40 nm dual-band 3-stream 802.11a/b/g/n/ac MIMO WLAN SoC with 1.1 Gb/s over-the-air throughput," in *IEEE Int. Solid-State Circuits Conf. (ISSCC) Dig. Tech. Papers*, Feb. 2014, pp. 350–351.
- [22] C. J. Fulton, "Digital array radar calibration and performance monitoring techniques for direct conversion and dual polarization architectures," Ph.D. dissertation, Dept. Elect. Comput. Eng., Purdue Univ., Lafayette, IN, USA, 2011.
- [23] C. Fulton and W. Chappell, "Calibration techniques for digital phased arrays," in *Proc. IEEE Int. Conf. Microw., Commun., Antennas Electron. Syst. (COMCAS)*, Nov. 2009, pp. 1–10.
- [24] S. Kalia, S. A. Patnaik, B. Sadhu, M. Sturm, M. Elbadry, and R. Harjani, "Multi-beam spatio-spectral beamforming receiver for wideband phased arrays," *IEEE Trans. Circuits Syst. I, Reg. Papers*, vol. 60, no. 8, pp. 2018–2029, Aug. 2013.
- [25] G. Kim, S. Joshi, C. M. Thomas, S. Ha, L. E. Larson, and G. Cauwenberghs, "A 1.3 mW 48 MHz 4 channel MIMO baseband receiver with 65 dB harmonic rejection and 48.5 dB spatial signal separation," *IEEE J. Solid-State Circuits*, vol. 51, no. 4, pp. 832–844, Apr. 2016.



- [26] S. Jain, Y. Wang, and A. Natarajan, "A 10 GHz CMOS RX frontend with spatial cancellation of co-channel interferers for MIMO/digital beamforming arrays," in *Proc. IEEE Radio Freq. Integr. Circuits Symp. (RFIC)*, May 2016, pp. 99–102.
- [27] L. Zhang, A. Natarajan, and H. Krishnaswamy, "A scalable 0.1-to-1.7 GHz spatio-spectral-filtering 4-element MIMO receiver array with spatial notch suppression enabling digital beamforming," in *IEEE Int. Solid-State Circuits Conf. (ISSCC) Dig. Tech. Papers*, Jan./Feb. 2016, pp. 166–167.
- [28] H. Krishnaswamy and L. Zhang, "Analog and RF interference mitigation for integrated MIMO receiver arrays," *Proc. IEEE*, vol. 104, no. 3, pp. 561–575, Mar. 2016.
- [29] L. Zhang, A. Natarajan, and H. Krishnaswamy, "Scalable spatial notch suppression in spatio-spectral-filtering MIMO receiver arrays for digital beamforming," *IEEE J. Solid-State Circuits*, vol. 51, no. 12, pp. 3152–3166, Dec. 2016.
- [30] L. Zhang and H. Krishnaswamy, "A 0.1-to-3.1 GHz 4-element MIMO receiver array supporting analog/RF arbitrary spatial filtering," in *IEEE Int. Solid-State Circuits Conf. (ISSCC) Dig. Tech. Papers*, Feb. 2017, pp. 410–411.
- [31] B. Allen and M. Ghavami, *Adaptive Array Systems: Fundamentals and Applications*. Hoboken, NJ, USA: Wiley, 2005.



**Linxiao Zhang** (S'13) received the B.S. degree in electrical and electronics engineering from Nanyang Technological University, Singapore, in 2011. He is currently pursuing the Ph.D. degree with the Electrical Engineering Department, Columbia University, New York, NY, USA.

He interned at MediaTek, San Jose, CA, USA, and Texas Instruments, Dallas, TX, USA, in 2013 and 2016. His current research interests include wideband/software-defined radio with an emphasis on multiple-antenna systems.

Mr. Zhang received the EE MS Award of Excellence from the Electrical Engineering Department, Columbia University, in 2013.



**Harish Krishnaswamy** (S'03–M'09) received the B.Tech. degree in electrical engineering from IIT Madras, Chennai, India, in 2001, and the M.S. and Ph.D. degrees in electrical engineering from the University of Southern California (USC), Los Angeles, CA, USA, in 2003 and 2009, respectively.

In 2009, he joined the Electrical Engineering Department, Columbia University, New York, NY, USA, where he is currently an Associate Professor and the Director of the Columbia High-Speed and Millimeter-Wave IC Laboratory (CoSMIC). In 2017,

he co-founded MixComm Inc., a venture-backed startup, to commercialize CoSMIC Laboratory's advanced wireless research. His current research interests include integrated devices, circuits, and systems for a variety of RF, mmWave, and sub-mmWave applications.

Dr. Krishnaswamy was a recipient of the IEEE International Solid-State Circuits Conference Lewis Winner Award for Outstanding Paper in 2007, the Best Thesis in Experimental Research Award from the USC Viterbi School of Engineering in 2009, the Defense Advanced Research Projects Agency Young Faculty Award in 2011, the 2014 IBM Faculty Award, and the 2015 IEEE Radio Frequency Integrated Circuits Symposium Best Student Paper Award (First Place). He has been a member of the technical program committee of several conferences, including the IEEE International Solid-State Circuits Conference since 2015 and the IEEE Radio Frequency Integrated Circuits Symposium since 2013. He currently serves as a Distinguished Lecturer for the IEEE Solid-State Circuits Society.